

Deep learning segmentation and quantification of Meibomian glands

Sahana M Prabhu*, Abhijith Chakiat**, Shashank S**

**Corresponding author. ** Both have contributed equally.*

Robert Bosch Engineering & Business Solutions, Bangalore, India.

(sahana.muraleedharaprabhu@in.bosch.com; abhijith4m0505@gmail.com; knhash@pm.me).

Krishna Poojita Vunnava, and Rohit Shetty

Narayana Nethralaya, Bangalore, India.

(vkpoojita@gmail.com; drrohitshetty@yahoo.com).

Abstract

Meibomian gland dysfunction is the most common cause of the dry-eye syndrome, and it refers to deterioration of the meibomian glands that are present in the eyelids. This paper presents a strategy for segmentation of meibomian glands using Convolutional Neural Networks. We also present a set of clinically-relevant metrics to quantify the health of the glands. In order to model the possible variations in data using a limited representative training image database, our work proposes several custom augmentation strategies to use the available data efficiently. We have collected Meibography images from two sources: (i) Oculus Keratograph-5M, which is a high-end table-top equipment, and (ii) Prototype Hand-held camera. We have found that the images captured from the hand-held imager are of sufficient quality and comparable to the Oculus Keratograph. We present the analysis of the results of gland segmentation on test-sets from both these imagers and compare against the results from ground-truth markings by clinical experts. Our deep learning-based segmentation model is tested on an equal number of diseased images as well as healthy images. We conclude that the metrics from our segmentation results are close to those derived from ground-truth, and also that the metrics are useful for differentiating between healthy versus diseased eyes.

Keywords: Meibography; Deep Learning; Image Segmentation; Convolutional neural networks.

1. Introduction

Meibomian glands have the function of secreting the vital lipid layer, which constitutes the outermost layer of the tear film. Meibomian gland dysfunction (MGD) constitutes about two-thirds of dry-eye disease and is associated with changes in glands, which can lead to low lipid secretion or obstruction of the ducts. These changes lead to variation in quality of lipid secretion and resultant excessive evaporation of tears and symptoms of dry-eye. One simple technique a doctor might use for the diagnosis of MGD is to apply pressure to the eyelid and thereby express the contents of the meibomian glands. Observing the quality of these secretions often can enable a trained eye care professional to determine if the patient has MGD. It is a condition brought on by constant exposure to visual display terminals, pollution, age-related risk and contact lens usage. This condition can lead to severe discomfort, interfering with daily activities, but it can be delayed/stopped if detected and treated at the early stages.

Machine learning (ML) techniques have emerged in biomedical sciences to improve detection of diseases, using image data alone. Learning can be supervised, weakly-supervised or unsupervised. Deep learning (DL) is part of a broader family of ML methods based on learning data representations, as opposed to task-specific algorithms [1]. Convolutional neural networks (CNN) have shown promise in both classification and segmentation problems in medical imaging. These DL approaches are very data-intensive, which can be satisfied by the enormous imagery present for the ocular diseases obtained from various devices. In this work, we have included image datasets from two devices: (i) Prototype hand-held modified Infrared fundus imager and (ii) Oculus Keratograph 5M, which is a high-end table top device used for Meibography. We have included training and testing sets from both equipment, and have shown that we achieve close accuracy in terms of metrics (with respect to ground-truth) for

even the images from the hand-held device.

Studying the morphology of the Meibomian glands requires segmenting out the glands from the meibography images of everted eyelids as well as quantifying the properties of the glands in the form of metrics. In this paper, we propose a deep learning-based approach for automatically segmenting the meibomian glands, based on pixel-wise convolutional neural networks. This work also presents the measurements of five clinically-relevant, quantitative metrics, which provide a clear distinction between healthy versus MGD-affected eyes. The novelty of the approach presented here lies in the following: (i) To the best of our knowledge, we are the first to propose a deep-learning network approach, which utilizes self-learned features rather than hand-crafted features (such as in [2]), for automatically segmenting the meibomian glands from infrared images. (ii) To present the details of several customized data augmentations that are relevant to gland segmentation. (iii) Quantitative analysis of the automatically segmented meibomian glands is performed in terms of a variety of metrics, unlike prior works which focus only on one metric, viz., drop-out [3]. The work-flow of our approach is outlined in Fig. 1.

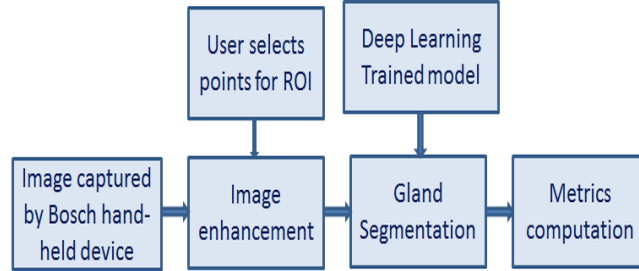


Figure 1: Flowchart of the meibography analysis system

Studies done on MGD have all widely studied only the gland dropout ratio as a metric for grading the disease severity, as described in [4] and [3]. However, it is noted that, in obstructive type of MGD, hyper-keratinization leads to progressive changes in the gland [5], [6]. Increased tortuosity, dilation of the gland lumen, widening of the gland, atrophy and fading of the glands are

often the sequential morphological alterations seen in the progression of MGD [7], especially in the early stages. We have taken these effects into account and have formulated a set of metrics that quantify the health of the glands in a more comprehensive manner. We evaluate the accuracy of our segmentation versus the ground-truth, in terms of these metrics, since the accuracy of the MGD diagnosis depends on these metrics.

This paper is organized as follows. Section 2 describes the survey of relevant previous literature. Section 3 gives the details of the annotated dataset and also describes the data augmentation schemes to increase the training set. Section 4 presents the methodology of applying the deep learning network. Section 5 analyzes the experimental results obtained in terms of the five metrics, and finally Section 6 presents the conclusions obtained from these results.

2. Related work

A procedure to detect meibomian glands algorithmically and then use them as features for classification of the images was proposed in [8]. Another approach for detection of MGD is by analyzing tear film maps, and a novel method for this purpose was presented in [9]. Scale- invariant feature transform (SIFT)[10], an algorithm to detect and describe local features in images, was used to represent the thickness or width of the glands. An objective approach to determine drop-out was described in [3]. Hand-crafted features based on Gabor filtering and support vector machine (SVM) were used for classification of MGD in [2].

Deep learning architectures such as convolution neural networks have been applied to various fields including computer vision, medical image analysis, bio-informatics, etc. The self-learned features have been proven to produce accurate results comparable to human observers. There are quite a few deep learning-based image segmentation methods that have shown promising results [11], [12].

Segmentation of objects from images can be performed in two ways: (i) Bounding box detection using sliding-window based approach, which was used, for example, to detect fetal abdomen from ultrasound images [13],(ii) Pixel-wise

segmentation by generating a binary mask of the object, used successfully for microscopic images [12]. Fully Convolutional Networks (FCNs) for Semantic segmentation [11] shows that pixel-wise convolutional networks are the state-of-the-art in semantic segmentation. Transforming fully connected layers into convolution layers enables the classification net to provide output in the form of a heat-map. Segmentation is a primary task in many biomedical applications such as vessel segmentation from angiograms [14].

The U-net segmentation architecture [12] is a modification of FCN [11] by using a large number of feature channels in the up-sampling step. Data augmentation by applying random elastic deformations is the key to train a segmentation network with very few annotated images [12]. Another notable architecture is the V-Net Architecture [15], for Volumetric Medical Image Segmentation, which is used to process the medical data used in clinical practice that consists of 3D volumes. A multi-input multi-output (MIMO) CNN [16] was proposed for segmentation of glands in histopathology images. This architecture [16] incorporates context by visualizing input and output at multiple resolutions. A review of computational image analysis for digital pathology [17] describes predictive modelling using detection and segmentation.

3. Description of datasets and augmentation

Our approach for pixel-wise segmentation of the glands uses a deep learning architecture to produce a binary segmentation map of the glands. This gland segmentation is then run through a quantification module that calculates the metrics such as tortuosity, number of glands, width, length and dropout of the glands, which are useful and clinically-relevant measures to predict the MGD. In this section, we provide the details of the dataset and augmentation schemes.

3.1. Datasets and ground-truth

The training image data of the everted eyelids was collected from various hospitals using: (i) Prototype Hand-held imager (ii) Oculus Keratograph 5M

[18]. Oculus device is an advanced corneal topographer with a built-in real keratometer and a color camera optimized for external imaging. The Bosch prototype device is a modified fundus camera that can capture infrared images, and is a compact, hand-held device, suitable for usage in screening camps. The dataset is comprised of 400 Bosch images and 400 Oculus images, all of which had ground truth gland segmentation marked by clinical experts. The same patients were imaged using both the devices so that a direct comparison across the cameras is feasible. The data was split into training set of 300 images from hand-held camera and 300 images from the table-top camera. The rest of the images comprised the test set, which has 50 diseased images and 50 healthy images from each device, hence there are totally 200 images used for testing.



Figure 2: (a) Image captured by prototype hand-held camera and (b) Enhanced image.

In order to improve the contrast of images, a customized image enhancement technique called Contrast Limited Adaptive Histogram Equalization (CLAHE) was used, wherein multiple histograms of distinct sections are used to re-distribute the contrast in the image. Note that Fig. 2(a) shows an example of the original image captured by the prototype hand-held device, and Fig. 2(b) shows the image after enhancement, wherein the glands are clearly visible. These enhanced images were used to train the deep learning model discussed in this section.

The ground truth (GT) for the training set had the glands segmented from enhanced images using Fiji tool in ImageJ software [19]. It was noted that, on

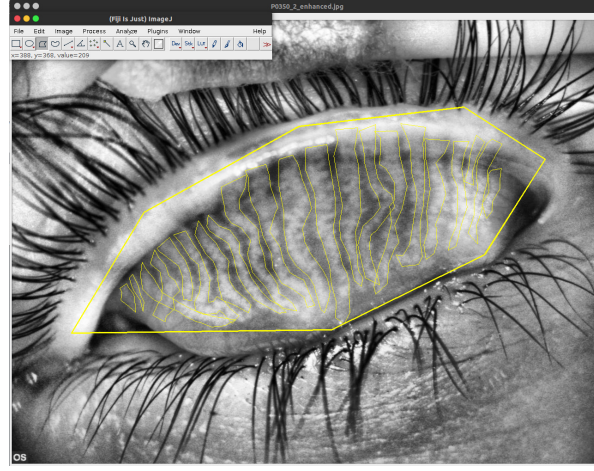


Figure 3: Glands and ROI marked using the polygon tool in Fiji.

an average, 5 minutes were required to mark glands for each image even for an expert. This was found to be a laborious process, and our algorithm aims at automating this procedure. Fiji provides a polygon tool that was used to select each gland separately by tracing out its boundary. The same procedure was repeated for the region of interest (ROI) by tracing it using the polygon tool. In order to bring in uniformity, the ROI is in the form of a hexagon, and only six points need to be marked as input. Figure 3 shows the ground-truth markings of glands and ROI. Note that ROI is only required for computation of one of the five metrics, viz. dropout, and is not used for training.

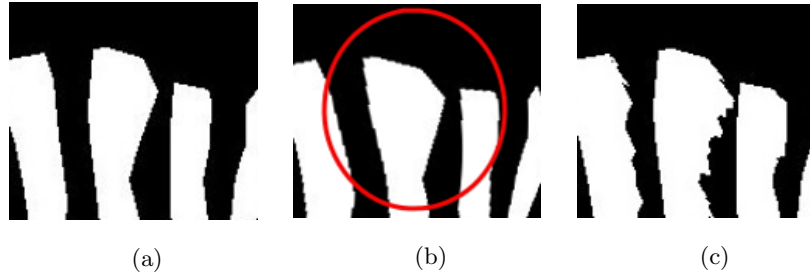


Figure 4: Enlarged gland maps for visualization of data transformations: (a) Original gland map. (b) After Elastic Transformation. (c) After Perturbation.

3.2. Data augmentation

Data augmentation is an approach for adding more data that is representative of the variations, if there are only few training samples available. Instead of applying common image transformations such as shift, rotation, and shear, we have explored customized transformations that reflect the characteristics of the glands. Since each gland is marked individually using free-hand tool, there is high scope for variations in the ground-truth markings, especially in diseased cases wherein the glands are more tortuous (such as the example in Fig. 2). In this work, we have considered two levels of data augmentation, which we found to be realistic variations of the data captured:

(i) Elastic transformation (ET): The glands do not have a uniform shape and there are different orientations for each gland. It is vital to capture this local distortion in augmentation. The training images are augmented using elastic transformation [20]. This involves applying a smoothing filter that reduces the high spatial frequencies in the data, which are mostly attributable to noise, and emphasizes the lower frequencies. The smoothing filter used here is the Gaussian filter which applies weights according to the Gaussian distribution [21]. According to [20], the elastic transformation also involves applying local distortions. Distortions such as translations, rotations, and skewing can be generated by applying affine displacement fields to images, pixel-wise rather than to the overall image. This is achieved by computing a new target location for every pixel with respect to its original location.

(ii) Perturbation (P): It was noted that there are minor variations in the way the ground-truth of the glands are marked (both inter-operator and intra-operator), and we have made an attempt to model this using perturbations. The perturbation of the images are done by extracting the contours of the glands and then incrementing the coordinates of the contours by a small random integer. This results in random perturbations along the perimeter of the gland.

The training data can be seen as three sets of images: (i) The original set of images forms one set (set A) of the training data. (ii) The set of images, that are elastic transformed, forms set B. (iii) The third set (set C) is obtained by ap-

plying perturbation to set A. Hence, the training set consists of: original images x , Elastic transformed images x , Perturbed images x . Hence, the total number of images in the training set is $x + x + x = 3x$, i.e., the data augmentation has tripled the training data. An example of the zoomed portion of the gland map is presented in Fig. 4(a), and the two data augmentation transformations applied to it are shown in Figs. 4 (b) and (c).

4. Segmentation and quantification methods

An adaptation of the U-Net network, which was first introduced in [12] for segmenting microscopic images, is used for our framework. A pictorial representation of the network is shown in Fig. 5, and it presents the details of the convolutional filters. The network consists of 19 convolutional layers in total, and from our experiments, we have found that it is the optimal number of layers for the problem at hand. The left side of the network is down-sampling path (as done for all CNN architecture), while the right side has an up-sampling path. The network uses the up-sampling part to propagate context information to the higher resolution layers. As mentioned in [12], up-sampling of the features is followed by 2x2 convolution, that halves the number of feature channels. This is followed by concatenating with the (corresponding) cropped features from the down-sampling path, and two 3x3 convolutions, each followed by Rectified Linear Unit (ReLU) activation functions. The down-sampling part doubles the number of feature channels. Skip connections link the encoder layers to the decoder layers that are on the same level, thereby concatenating the local information.

All the layers, except the last one, use a Rectified Linear Unit (ReLU) as the activation function. The ReLU activation function is defined as follows, and is used for CNN in general, to mitigate the vanishing gradient problem:

$$f(x) = \max(0, x) \quad (1)$$

The last convolutional layer alone uses a soft-max function, that is used for getting the output binary labels for each pixel of the gland images. The

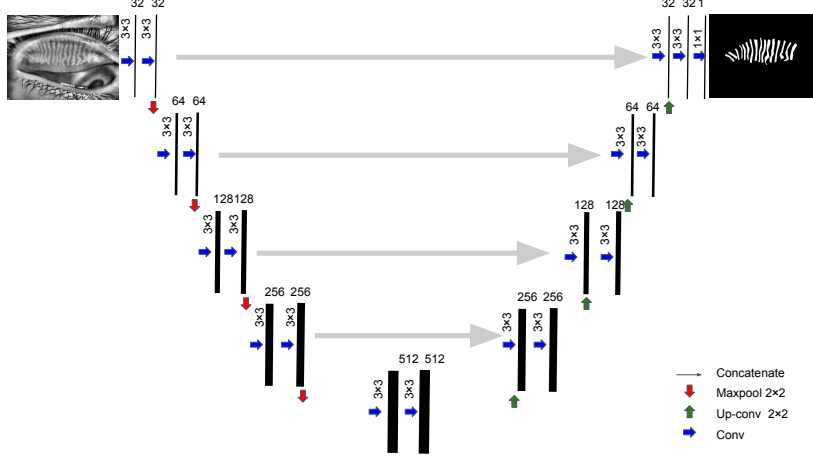


Figure 5: Network architecture: Test case is enhanced image, and output is gland map.

soft-max function is specified as follows:

$$f(v_i) = \frac{e^{v_i}}{\sum_j e^{v_j}} \quad (2)$$

where v_i denotes the elements in the output layer.

Since this is pixel-wise binary segmentation, we have attempted two loss functions that are applicable: (i) Dice coefficient: the ratio of intersection over union, and is intuitively more suitable for larger objects with single continuous border, and (ii) Binary cross-entropy: useful for gland segmentation, wherein there are slight pixel-wise deviations in the multiple unconnected components. During training, we found that the latter gave more accurate segmentation results. This is due to the fact that the gradient of cross-entropy has a stable form when compared to Dice coefficient (wherein small denominator values can cause unstable solution and convergence curve is not smooth). The binary cross-entropy loss function is defined as:

$$H_y I(y) = \sum_i y_i I(\log(y_i)) \quad (3)$$

which penalizes, at each position, the deviation from unity. The images were reduced to one-fourth the size, to speed up training. The network is trained

for 300 epochs, beyond which the residue of the loss function did not show any significant change. The same deep learning architecture was trained with (i) images with No Augmentation (NA) and (ii) with augmented images that underwent Elastic Transformation (ET), (iii) the third model that was found most accurate, uses the data that includes ET and Perturbation (P). Note that there are equal number of healthy and diseased cases in the non-augmented set itself, so there is no class imbalance issue. This was done to compare the effect of the data augmentations, and the results of these three models are shown in Section 5.

4.1. Meibomian metrics

After obtaining the output gland segmentation binary maps, we apply five clinically-relevant metrics derived from the meibomian glands that provide quantification for MGD: (i) Dropout (ii) Tortuosity (iii) Width, (iv) Length, and (v) Number of glands. Note that for all metrics (except dropout), the connected components in the binary gland segmentation map are used. The formulae for each of these are defined in this sub-section, and a graphical illustration is provided in Fig. 6 (see online color version).

4.1.1. Dropout

The dropout is the ratio of the gland dropout area to the total area of the ROI. Note that the ROI was marked using six points, to form a hexagonal polygon. The gland dropout area is calculated as follows:

$$\text{Dropout} = \frac{\text{Total area} - \text{Gland area}}{\text{Total area}} \quad (4)$$

and represented by the blue-colour area in Fig. 6 (see online color version). This parameter is most important as it directly measures the area of coverage of the glands. More than 50% dropout is indicative of deteriorating glands.

4.1.2. Tortuosity

Tortuosity is the property that defines the twist of a curve. A simple mathematical method to measure tortuosity is arc-to-chord ratio, which is the ratio

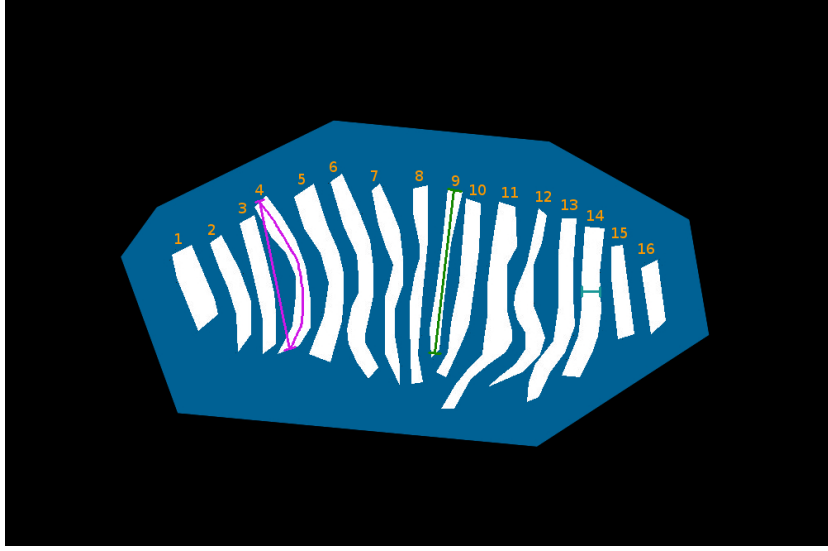


Figure 6: Visualization of the metrics: Dropout area, Tortuosity (Gland 4), Width (Gland 14), Length (Gland 9), Number of glands.

of the length of the curve to the distance between the end points.

$$\text{Tortuosity} = \frac{\text{Arclength}}{\text{Distance between Endpoints}} \quad (5)$$

The arc-to-chord ratio equals unity for a straight line and is infinite for a circle. In Fig. 6, the purple curve represents the arc-length of the gland. while the straight line joining the end-points represents the corresponding chord length (zoom twice and view the online color version). Distortion of the glands, which happens even at early stages, is quantified by this metric.

4.1.3. Width

The width of each gland is measured in pixels at the mid-line of the image as shown in Fig. 6 (gland 14, marked in cyan - see online color version), The average width of the meibomian glands is computed as a metric.

4.1.4. Length

From the gland segmentation map, we find the skeletonized components, so that each gland is reduced to one-pixel width. The arc-length of each gland

gives pixel-wise length, and the average length of the glands is taken. In Fig. 6, the green line across gland 9 shows the length of one gland. If the glands deteriorate, then the length decreases.

4.1.5. Number of glands

The total number of individual glands in the binary mask is computed using the number of connected components present in the binary gland map (refer Fig. 6 glands 1-14, see the numbers on top of each gland). In diseased cases, the glands drop and also merge, which reduces number of glands.

It is important to note that length and width are the parameters that depend on the resolution of the image (and can be scaled accordingly), whereas the other metrics represent ratios or count, and thus independent of resolution.

5. Experimental results

The testing dataset includes prototype and Oculus sets, each divided into healthy and diseased sets. The prototype test set consists of 50 healthy images and 50 diseased images. Similarly, the count of healthy and diseased images in the Oculus test dataset is 50 and 50, respectively. In order to maintain consistency, the same patients who had their everted eyelids imaged by the prototype hand-held imager, were also enrolled for capturing images using the Oculus table-top Keratograph.

For the test dataset, the metrics from the automatically segmented glands are compared with the metrics from the marked ground-truth. The three trained models: (i) No Augmentation (NA), (ii) Original data and elastic transformed (ET) data (iii) Data with ET and Perturbation (ETP), were tested using the test dataset. A summary of the metrics are shown in Tables 1-4, for the four categories: (i) Diseased cases imaged by prototype camera, (ii) Diseased images from Oculus, (iii) Healthy eyes captured by prototype imager, and (iv) Healthy cases from Oculus instrument. Average of metrics for GT versus ETP, and also only ET and with no augmentation are presented in Tables 1-4, and the p-value

(using two-sample t-test, assuming equal variances) between ETP versus GT is also presented.

Table 1: Diseased test images (Bosch prototype): p-value between GT versus ETP

Metrics	GT	ETP	ET	NA	p-val
No. glands	11.11 ± 4.88	13.11 ± 3.16	14.40 ± 3.28	18.43 ± 5.26	0.028
Tortuosity	1.23 ± 0.17	1.29 ± 0.19	1.23 ± 0.09	1.25 ± 0.08	0.024
Width	4.32 ± 0.73	4.30 ± 0.42	4.16 ± 0.33	4.22 ± 0.35	0.906
Length	42.34 ± 10.65	40.31 ± 10.39	34.19 ± 8.97	30.57 ± 7.93	0.379
Drop-out	0.69 ± 0.14	0.67 ± 0.12	0.73 ± 0.12	0.76 ± 0.12	0.358

Table 2: Diseased test images (Oculus): p-value between GT versus ETP

Metrics	GT	ETP	ET	NA	p-value
No. glands	13.1 ± 4.82	11.8 ± 3.97	12.37 ± 4.17	15.22 ± 4.92	0.207
Tortuosity	1.24 ± 0.23	1.32 ± 0.11	1.44 ± 0.29	1.40 ± 0.22	0.030
Width	4.17 ± 0.66	4.30 ± 0.50	4.40 ± 0.47	4.41 ± 0.44	0.199
Length	46.22 ± 10.24	45.59 ± 11.57	42.41 ± 10.52	36.92 ± 9.35	0.817
Drop-out	0.66 ± 0.10	0.62 ± 0.14	0.64 ± 0.11	0.69 ± 0.12	0.051

Table 3: Healthy test images (Bosch prototype): p-value between GT versus ETP

Metrics	GT	ETP	ET	NA	p-value
No. glands	15.89 ± 4.06	14.40 ± 3.41	15.22 ± 3.42	20.81 ± 4.28	0.036
Tortuosity	1.24 ± 0.16	1.31 ± 0.11	1.33 ± 0.16	1.26 ± 0.13	0.039
Width	4.29 ± 0.55	4.20 ± 0.51	4.11 ± 0.41	4.05 ± 0.39	0.381
Length	51.14 ± 9.39	47.88 ± 11.05	43.79 ± 8.34	37.03 ± 9.32	0.093
Drop-out	0.54 ± 0.08	0.55 ± 0.06	0.60 ± 0.06	0.64 ± 0.09	0.327

It is evident that the average metric of the model trained with data which included perturbed and elastic transformed images is close to the average metrics of GT. Also, the p-values with respect to GT in all the cases are > 0.005 ,

Table 4: Healthy test images (Oculus): p-value between GT versus ETP

Avg. Metrics	GT	ETP	ET	NA	p-value
No. glands	16.9 ± 3.95	14.16 ± 3.61	14.52 ± 3.88	18.02 ± 4.49	0.500
Tortuosity	1.21 ± 0.15	1.29 ± 0.13	1.44 ± 0.25	1.35 ± 0.15	0.071
Width	3.86 ± 0.53	4.17 ± 0.50	4.12 ± 0.38	4.20 ± 0.34	0.236
Length	55.12 ± 9.13	54.40 ± 9.34	48.73 ± 9.34	44.70 ± 9.94	0.893
Drop-out	0.59 ± 0.08	0.56 ± 0.07	0.58 ± 0.06	0.63 ± 0.07	0.084

which shows they are close. The average metrics from the other two models trained with only elastic transformed images and with no data augmentation did not quite match with the ground truth results. This proves that the two data augmentation strategies have contributed to improving the accuracy of the trained model, and represent the real-case variations in the data.

The metrics for the four datasets have been compared and visualized across the deep learning output and the ground truth images in the form of box plots from Fig. 7-11. Each of these figures contains plots corresponding to the metrics - (a) Dropout, (b) Tortuosity, (c) Width, (d) Length, (e) Total number of glands. Each plot gives a visual comparison of the respective metric between the deep learning output and the ground truth measures.

We have presented two examples of the deep learning output gland maps in Figs. 12-13. Note that Fig. 12(a) is the test input enhanced image of a healthy eyelid, and the gland map in Fig. 12(b) shows that the glands cover the eyelid in a uniform manner, most of the glands extend from top to bottom of the eyelid. Figure 13(a) shows a diseased test enhanced image, and the corresponding output gland map in Fig. 13(b) correctly shows that glands are missing at some portions of the eyelid, and most of the existing glands are tortuous and disjointed. Visually observing the input image and output from our model, it is apparent that the gland segmentation is captured well, even for diseased cases, wherein the glands are fading out.

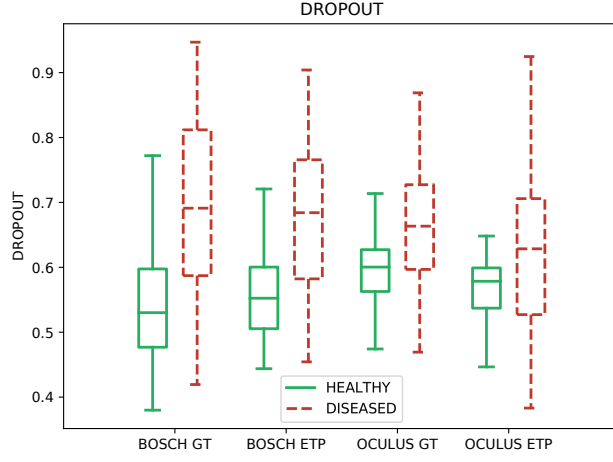


Figure 7: Dropout in healthy and diseased cases across Bosch and Oculus datasets

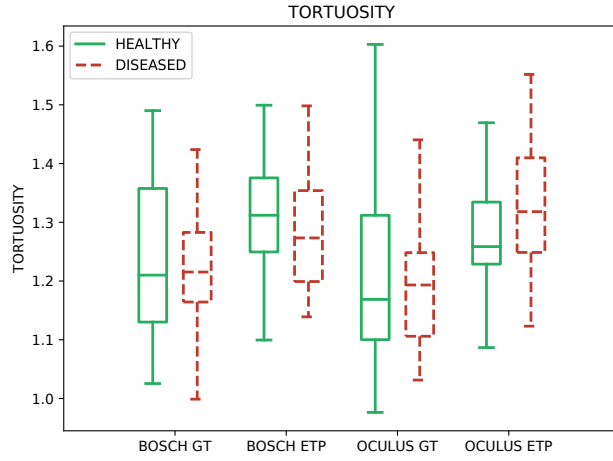


Figure 8: Tortuosity in healthy and diseased cases across Bosch and Oculus datasets

6. Discussion and Conclusion

We are the first to propose an automated algorithm based on deep learning for segmentation of meibomian glands and also to evaluate various features for quantification of these glands. In this section, we summarize the results presented in Tables 1-4, and the plots depicted in Figures 7-11. There are

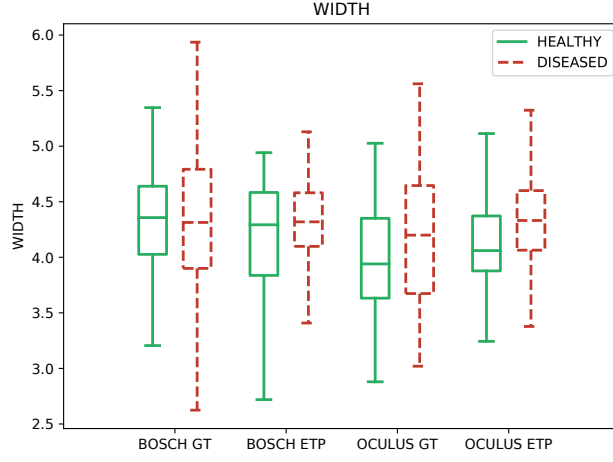


Figure 9: Width of glands in healthy and diseased cases across Bosch and Oculus datasets

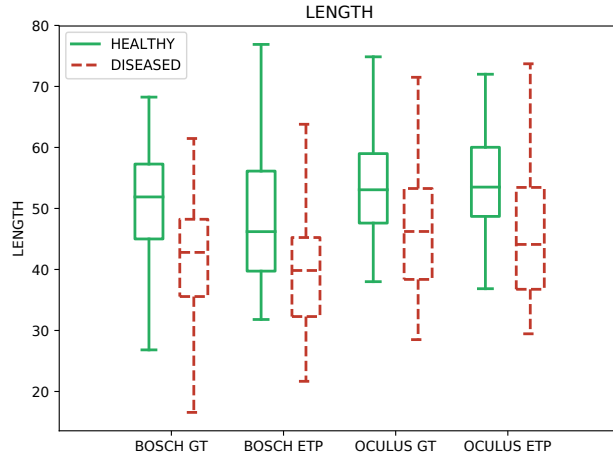


Figure 10: Length of glands in healthy and diseased cases across Bosch and Oculus datasets

several comparisons that we have attempted here, which are outlined as follows.

(i) Comparing GT results with those from the automatic gland segmentation algorithm, we can conclude that all the five metrics are quite comparable. In addition, we have observed that adding both perturbations and elastic deformations as data transformations have contributed to closer match with GT.

(ii) It is found that the dropout for the healthy cases is lower than that of

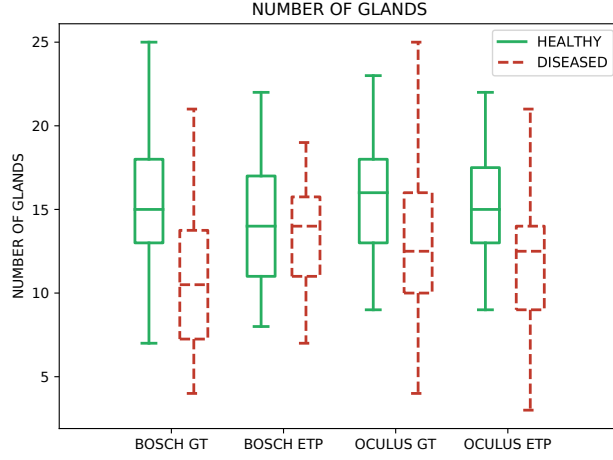


Figure 11: Number of glands in healthy and diseased cases across Bosch and Oculus datasets

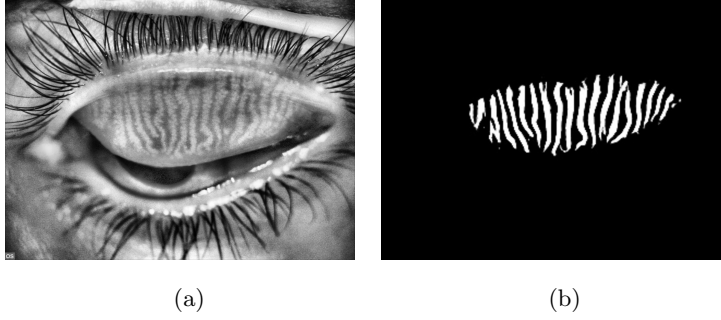


Figure 12: Example: (a) Healthy image (from prototype). (b) Gland map output.

the diseased cases, as expected. The average of length of glands for healthy sets is significantly greater than that of the diseased set, which show that glands get shortened as they deteriorate. The tortuosity of diseased glands is greater than that of healthy cases. The number of glands in healthy cases is greater than in diseased patients, as the glands start to drop off.

(iii) Test-set images were taken from Bosch hand-held and Oculus Keratograph imagers from the same patients (at different positions) in order to enable a direct comparison. It is observed from Figures 7-11 that the metrics resulting from the Bosch data are quite comparable in range to the Oculus data.



Figure 13: Example: (a) Diseased image (from prototype). (b) Gland map output.

In conclusion, we have presented a deep learning-based approach for the automatic segmentation of meibomian glands, which, to our knowledge, is the first attempt of its kind in Meibography. We have also analyzed five clinically relevant metrics in a detailed manner, and found that they are representative of the changes that are associated with MGD. Comparison of the results from images captured by Bosch hand-held imager with those of the Oculus Keratograph show that the images are equivalent for the analysis of MGD, and the algorithm developed by Bosch is an efficient and quantified accurate approach for usage in clinical settings for the analysis of MGD.

Automated gland segmentation and deep learning can make the management of MGD more widespread. Alterations in the number of glands, tortuosity and gland length are early indicators of the disease, at which point it is more amenable to various treatment options. Use of artificial intelligence and success of neural networks is the future of medical diagnostics.

Acknowledgment

This work was internally supported by Robert Bosch Engineering and Business Solutions, Bangalore, India. The reference number of IRB approval of this study is *C/2017/01/009*.

References

- [1] D. Ravi, C. Wong, F. Deligianni, M. Berthelot, J. Andreu-Perez, B. Lo, G.-Z. Yang, Deep learning for health informatics, *IEEE journal of biomedical and health informatics* 21 (1) (2017) 4–21.
- [2] T. Celik, H. K. Lee, A. Petznick, L. Tong, Bioimage informatics approach to automated meibomian gland analysis in infrared images of meibography, *Journal of optometry* 6 (4) (2013) 194–204.
- [3] R. Arita, J. Suehiro, T. Haraguchi, R. Shirakawa, H. Tokoro, S. Amano, Objective image analysis of the meibomian gland area, *British Journal of Ophthalmology* (2013) bjophthalmol–2012.
- [4] H. Pult, B. Riede-Pult, Comparison of subjective grading and objective assessment in meibography, *Contact Lens and Anterior Eye* 36 (1) (2013) 22–27.
- [5] E. Knop, N. Knop, Meibomian glands: part iv. functional interactions in the pathogenesis of meibomian gland dysfunction (mgd), *Der Ophthalmologe: Zeitschrift der Deutschen Ophthalmologischen Gesellschaft* 106 (11) (2009) 980–987.
- [6] A. Bron, J. Tiffany, The contribution of meibomian disease to dry eye, *The ocular surface* 2 (2) (2004) 149–164.
- [7] E. Knop, N. Knop, T. Millar, H. Obata, D. A. Sullivan, The international workshop on meibomian gland dysfunction: report of the subcommittee on anatomy, physiology, and pathophysiology of the meibomian gland, *Investigative ophthalmology & visual science* 52 (4) (2011) 1938–1978.
- [8] Y. W. Koh, T. Celik, H. K. Lee, A. Petznick, L. Tong, Detection of meibomian glands and classification of meibography images, *Journal of biomedical optics* 17 (8) (2012) 0860081–0860087.

- [9] B. Remeseiro, A. Mosquera, M. G. Penedo, Casdes: a computer-aided system to support dry eye diagnosis based on tear film maps, *IEEE journal of biomedical and health informatics* 20 (3) (2016) 936–943.
- [10] D. G. Lowe, Object recognition from local scale-invariant features, in: *IEEE International Conference on Computer Vision (ICCV)*, Vol. 2, 1999, pp. 1150–1157.
- [11] J. Long, E. Shelhamer, T. Darrell, Fully convolutional networks for semantic segmentation, in: *Proc. IEEE Conf. Computer Vision and Pattern Recognition (CVPR)*, 2015, pp. 3431–3440.
- [12] O. Ronneberger, P. Fischer, T. Brox, U-net: Convolutional networks for biomedical image segmentation, in: *Intl. Conf. Medical Image Computing and Computer-Assisted Intervention (MICCAI)*, Springer, 2015, pp. 234–241.
- [13] H. Ravishankar, S. M. Prabhu, V. Vaidya, N. Singhal, Hybrid approach for automatic segmentation of fetal abdomen from ultrasound images using deep learning, in: *IEEE International Symposium on Biomedical Imaging (ISBI)*, IEEE, 2016, pp. 779–782.
- [14] E. Nasr-Esfahani, N. Karimi, M. H. Jafari, S. M. R. Soroushmehr, S. Samavi, B. Nallamotheu, K. Najarian, Segmentation of vessels in angiograms using convolutional neural networks, *Biomedical Signal Processing and Control* 40 (2018) 240–251.
- [15] F. Milletari, N. Navab, S.-A. Ahmadi, V-net: Fully convolutional neural networks for volumetric medical image segmentation, in: *International Conference on 3D Vision (3DV)*, 2016, pp. 565–571.
- [16] S. E. A. Raza, L. Cheung, D. Epstein, S. Pelengaris, M. Khan, N. M. Rajpoot, Mimonet: Gland segmentation using multi-input-multi-output convolutional neural network, in: *Annual Conference on Medical Image Understanding and Analysis*, Springer, 2017, pp. 698–706.

- [17] A. Madabhushi, G. Lee, Image analysis and machine learning in digital pathology: Challenges and opportunities, *Medical image analysis* 33 (2016) 170–175.
- [18] <https://www.oculus.de/us/products/topography/topography/keratograph-5m/highlights/>, oculus keratograph, last accessed on 03 nov 2018.
- [19] J. Schindelin, I. Arganda-Carreras, E. Frise, V. Kaynig, M. Longair, T. Pietzsch, S. Preibisch, C. Rueden, S. Saalfeld, B. Schmid, et al., Fiji: an open-source platform for biological-image analysis, *Nature methods (Nature Research)* 9 (7) (2012) 676–682.
- [20] P. Y. Simard, D. Steinkraus, J. C. Platt, et al., Best practices for convolutional neural networks applied to visual document analysis., in: *ICDAR*, Vol. 3, 2003, pp. 958–962.
- [21] M. Hall, Smooth operator: Smoothing seismic interpretations and attributes, *The Leading Edge, Society of Exploration Geophysicists* 26 (1) (2007) 16–20.